eChem
https://www.sciltp.com/journals/eChem

Article

Green Valorization of Seawater via Homogeneous Nucleation Electrochemistry: Synthesis of Nano-$CaCO_3$ and $Mg(OH)_2$ Adsorbents for Heavy Metal Removal

Yuchen Zhao [1], Wenda Kang [1,2,*], Shuixiang Xie [3,4], Yidong Ruan [1], Xiang Zhou [1], Weilong Wang [1], Yongqian Zhang [5], Hongtao Yu [1] and Gong Zhang [2]

[1] Key Laboratory of Industrial Ecology and Environmental Engineering (Ministry of Education), School of Environmental Science and Technology, Dalian University of Technology, Dalian 116024, China
[2] Center for Water and Ecology, State Key Laboratory of Regional Environment and Sustainability, School of Environment, Tsinghua University, Beijing 100084, China
[3] State Key Laboratory of Petroleum Pollution Control, Beijing 102206, China
[4] CNPC Research Institute of Safety & Environment Technology, Beijing 102206, China
[5] Erdos Power Supply Branch, Inner Mongolia Power (Group) Corporation Limited, Ordos 017000, China
* Correspondence: kangwd@mail.tsinghua.edu.cn

How To Cite: Zhao, Y.; Kang, W.; Xie, S.; et al. Green Valorization of Seawater via Homogeneous Nucleation Electrochemistry: Synthesis of Nano-$CaCO_3$ and $Mg(OH)_2$ Adsorbents for Heavy Metal Removal. *eChem* **2025**, *1*(1), 5. https://doi.org/10.53941/echem.2025.100005.

Received: 18 October 2025
Revised: 7 November 2025
Accepted: 14 November 2025
Published: 21 November 2025

Abstract: Rapid industrialization posed a serious threat to water safety due to heavy metal pollution, creating an urgent need for a green and efficient remediation solution. This research, leveraging electrocatalytic technology, innovatively proposes an electrochemical homogeneous nucleation strategy for the selective recovery of Ca^{2+} and Mg^{2+} from seawater. Through employing pH-controlled sequential precipitation, this strategy enables the synthesis of nano-$CaCO_3$ (BET surface area: 50.4 m^2/g) and nano-$Mg(OH)_2$ (109.8 m^2/g), which serve as high-performance adsorbents for efficient heavy metal removal. Both adsorbents demonstrated adsorption behaviors well-fitted to the Langmuir model, exhibiting exceptional maximum adsorption capacities for Cu(II) (838.2–1331.0 mg/g), Pb(II) (2180.5–3696.8 mg/g), Cd(II) (1065.3–1997.4 mg/g), and Cr(III) (424.1–637.5 mg/g). When configured as fixed-bed columns, the adsorbents reduced effluent concentrations of Cu(II), Pb(II), Cd(II), and Cr(III) to below 0.7 μg/L, meeting World Health Organization drinking water standards. Life cycle assessment revealed the electrochemical strategy reduced carbon emissions by 50–80% compared to conventional methods, achieving net-negative emissions (−10.428 kg CO_2eq per ton of water) when incorporating resource recovery benefits. This approach represents a synergistic solution for both resource utilization and environmental remediation, demonstrating significant potential for sustainable water treatment and circular economy development.

Keywords: electrocatalysis, seawater; resource recovery; metal adsorption; life cycle assessment

1. Introduction

With the acceleration of global industrialization, heavy metal pollution became a severe environmental challenge. Heavy metal ions such as Cu(II), Pb(II), Cd(II), and Cr(III) in industrial wastewater posed a significant threat to ecosystems and human health because of their toxicity, persistence, and bioaccumulation [1,2]. The World Health Organization set limits for these metal ions in drinking water at only 10–50 μg/L [3], while actual industrial effluent concentrations often reached mg/L levels, far exceeding safe thresholds [4]. It was estimated that over 400

million people worldwide faced health risks from heavy metal-contaminated water, especially in developing countries [5].

Among various heavy metal treatment techniques, adsorption was widely adopted because of its simplicity, moderate cost, and high efficiency. $CaCO_3$ [6] and $Mg(OH)_2$ [7] were regarded as environmentally friendly adsorbents, and nano-scale $CaCO_3$ and $Mg(OH)_2$ [8,9] received particular attention due to their high specific surface area and abundant surface active sites, which enabled effective capture of heavy metal ions through mechanisms such as surface complexation, ion exchange, and precipitation [10]. However, traditional methods for preparing adsorbents relied on mineral extraction and high-temperature calcination, which not only caused ecological damage but also produced large amounts of carbon emissions. Research showed that the production of one ton of conventional $CaCO_3$ emitted approximately 0.8 t CO_2 [11], while the production of $Mg(OH)_2$ was an energy-intensive process that typically required temperatures between 800 and 1000 °C [12]. Furthermore, adsorbents produced by these methods exhibited irregular morphology and a wide size distribution, failing to meet the requirements for high-efficiency adsorption.

Seawater, as an abundant natural resource, contained approximately 1.3 g/L of Mg^{2+} and 0.4 g/L of Ca^{2+}, thereby providing an ideal source for the sustainable extraction of these elements [13]. The electrochemical method demonstrated unique advantages in the utilization of seawater resources owing to its simple process, mild reaction conditions, and ease of control [14]. Compared with conventional chemical precipitation methods, the electrochemical method does not require the addition of extra reagents and reduces the risk of secondary pollution [15]. Its environmental friendliness was further enhanced by the increasing share of renewable energy in electricity generation. However, existing electrochemical technologies faced challenges such as electrode scaling, high energy consumption, and difficulty in separating Ca^{2+} and Mg^{2+}, while a systematic evaluation from a life cycle perspective was lacking.

To address these issues, we developed an electrochemical approach based on homogeneous nucleation. We utilized the nylon nets to isolate the anode acid solution, and the mesh cathode took advantage of the property that it could facilitate the diffusion of OH^-. With an optimized electrode design and precise control of the operating conditions, this process selectively extracts Ca^{2+} and Mg^{2+} from seawater and yields nano-adsorbents with controllable morphology. The method relied on local pH changes induced by the electrode and operated at ambient temperature and pressure without the addition of chemical reagents. The study systematically examined the adsorption performance and mechanism of the produced nano-$CaCO_3$ and nano-$Mg(OH)_2$ for various heavy metal ions. And for the first time, performed a comprehensive life cycle assessment of the electrochemical extraction process, quantifying resource consumption, energy requirements, and environmental impacts in comparison with conventional production methods. This study provided a new approach for the high-value utilization of seawater resources and offered theoretical and technical support for the sustainable development of environmentally friendly adsorbents.

2. Materials and Methods

2.1. Materials and Reagents

The seawater used in the experiments was collected from the coast of the East China Sea. The concentrations of various ions in seawater are shown in Table S1. The samples were filtered through 0.45 μm membranes to remove suspended solids before use. The simulated wastewater containing heavy metals was prepared by dissolving analytical-grade $Pb(NO_3)_2$, $Cd(NO_3)_2$, $Cu(NO_3)_2$, and $Cr(NO_3)_3$ in ultrapure water with a resistivity of 18.2 MΩ·cm. Anionic nitrate metal salts were specifically selected to ensure experimental consistency, as preliminary studies revealed significant counterion effects on adsorption performance, with copper adsorption capacities varying in the order $CuSO_4 > CuCl_2 > Cu(NO_3)_2$ due to different anion coordination abilities and ionic interactions (Figure S1). This standardization eliminates counterion interference and allows for accurate comparison of intrinsic metal-specific adsorption behaviors.

2.2. Electrochemical Extraction System

The electrochemical extraction system used a custom-designed mesh electrode module. It consisted of a tightly stacked assembly (all measuring 100 × 100 mm) comprising a stainless steel mesh cathode, a nylon net separator, and a ruthenium-iridium-titanium anode (Figure S2). The electrochemical reactor was made of acrylic panels with an effective volume of 400 mL. The mesh electrode module was mounted vertically, dividing the reactor into a 350 mL cathode chamber (extraction of calcium and magnesium ions) and a 50 mL anode chamber. To promote mass transfer, a magnetic stirrer was used in the cathode chamber at 500 revolutions per minute (RPM).

A DC power supply provided a stable current, and a pH probe was placed in the solution to monitor pH. Solution samples were taken at intervals, filtered through syringe-type membranes, and analyzed. Pure CO_2 (99.9%) was bubbled into the cathode chamber via a diffuser at 20 mL/min.

2.3. Selective Extraction of $CaCO_3$ and $Mg(OH)_2$

This study employed a pH-controlled two-stage electrolysis strategy to achieve the selective extraction of $CaCO_3$ and $Mg(OH)_2$. A nylon net separator was used to separate the anode and cathode chambers, preventing interference from acidic conditions in the anode and maintaining an alkaline environment in the cathode. Initially, seawater was introduced into the cathode chamber and electrolyzed at a low current density (0.5 mA/cm^2) while CO_2 was supplied. The cathodic reaction $2H_2O + 2e^- \rightarrow H_2 + 2OH^-$ increased the local pH, promoting CO_2 dissolution to form CO_3^{2-}, which then precipitated with Ca^{2+} to form $CaCO_3$ at pH 9.0–9.5. This pH range, the CO_2 reaction with cathodic OH^- shifts HCO_3^- toward CO_3^{2-} in the bulk, creating moderate $CaCO_3$ supersaturation while avoiding $Mg(OH)_2$ precipitation at higher pH. After most Ca^{2+} was consumed, the process entered the second stage: the current density was increased to 15 mA/cm^2 with no further CO_2 input. Continued electrolysis raised the pH to 10.5–13.0, leading to the precipitation of $Mg(OH)_2$ via reaction between Mg^{2+} and OH^- (Figure 1a). It is noteworthy that the particle size of $CaCO_3$ increased with prolonged reaction time; controlling electrolysis to 3–5 min yielded nano-scale particles (Figure S3), whereas extended duration resulted in micro-sized aggregates. In contrast, $Mg(OH)_2$ naturally formed nano-scale precipitate without strict time control. All runs were performed at 25 ± 1 °C with stirring at 500 rpm. After each precipitation stage, the solids were collected by filtration to isolate the target products. To quantify removal, solution samples were taken every 15 min to measure Ca^{2+}/Mg^{2+} and calculate extraction efficiency. To quantify the time-dependent change in $CaCO_3$ particle size, we extracted particle-size distributions from the SEM images at 1, 3, 5, 10, 15, and 30 min (Figure S4). At 1–3 min, the distribution lies in the range of 100–200 nm with good dispersion. At 5 min, it shifts to 1–3 μm, indicating the onset of aggregation and secondary growth. At 10–15 min, it broadens to 2–10 μm with clear aggregation. At 30 min, 10–80 μm aggregates appear, and the long tail becomes more pronounced. These trends are consistent with the SEM observations, supporting selecting 3–5 min as the optimal morphology window for $CaCO_3$.

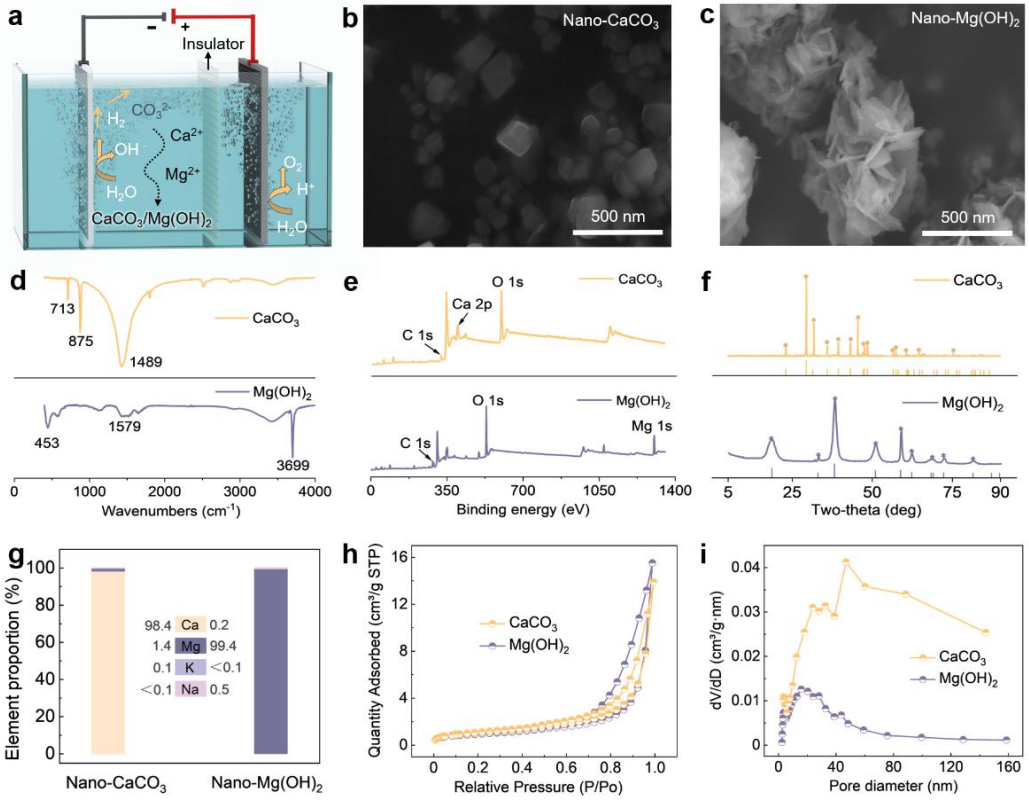

Figure 1. (**a**) Schematic illustration of electrochemical extraction process; SEM images of (**b**) nano-$CaCO_3$ and (**c**) nano-$Mg(OH)_2$; (**d**) FTIR spectra; (**e**) XPS survey spectra; (**f**) XRD patterns and the standard references for Calcite-type $CaCO_3$ (PDF #05–0586) and Brucite-type $Mg(OH)_2$ (PDF #44–1482); (**g**) Elemental composition analysis of nano-$CaCO_3$ and nano-$Mg(OH)_2$; (**h**) Nitrogen adsorption and desorption curves; and (**i**) Pore size distribution curves of nano-$CaCO_3$ and nano-$Mg(OH)_2$.

To visualize the bulk pH field and confirm bulk-dominated nucleation, we performed a dye-tracing test in a 27 L tank using thymolphthalein: the blue color first appeared in the bulk and rapidly filled the volume, with no localized aggregation of the blue color observed near the electrodes (70 s, 210 s, and 15 min; Figure S5). In addition, to isolate the effect of current from time, we screened current density at a fixed residence time of 3 min and measured the resulting pH (Stage-1: 0.1–1.0 mA/cm^2; Stage-2: 10–20 mA/cm^2). When the residence time was 3 min, the pH in the cathode region increased steadily with increasing current density (Figure S6). Therefore, a current density of 0.5 mA/cm^2 was selected for collecting nano-$CaCO_3$, and 15 mA/cm^2 for collecting nano-$Mg(OH)_2$.

2.4. Characterization

The major ionic composition of the seawater was determined by inductively coupled plasma atomic emission spectrometry (ICP-MS) [16] (The detailed information of the instrument can be found in Table S2). The collected $CaCO_3$ and $Mg(OH)_2$ precipitates were thoroughly washed with ultrapure water and subsequently dried in a vacuum oven at 60 °C for 24 h prior to characterization. Scanning electron microscopy (SEM, SU8600, Hitachi Ltd. (Tokyo, Japan)) was used to observe the surface morphology, and energy-dispersive X-ray spectroscopy (EDS, SU8600, Hitachi Ltd.) was conducted to analyze the elemental composition. X-ray diffraction (XRD, D8 ADVANCE, Bruker Corporation (Billerica, MA, USA)) was performed to determine the crystalline phases, while X-ray photoelectron spectroscopy (XPS, Axis Supra+, Kratos Analytical Ltd. (Manchester, UK)) was employed to examine the surface chemical states. Nitrogen adsorption-desorption measurements (BET, ASAP-2425, Micromeritics Instrument Corporation (Norcross, GA, USA)) were used to determine the specific surface area and pore structure. Fourier-transform infrared spectroscopy (FTIR, EQUINOX55, Bruker Corporation) was carried out to identify the surface functional groups.

2.5. Heavy Metal Adsorption and Calculation

Batch adsorption experiments were carried out to evaluate the performance of the prepared $CaCO_3$ and $Mg(OH)_2$ for Cu(II), Pb(II), Cd(II), and Cr(III). Initial metal concentrations ranged from 1 to 2000 mg/L. A fixed adsorbent dosage of 0.5 g/L was used. The pH was adjusted to 5.5–6.0 with 0.1 mol/L HNO_3 and 0.1 mol/L NaOH. Suspensions were shaken at 25 °C.

Continuous-flow performance was assessed in a packed-bed column. A cylindrical acrylic column (internal diameter 20 mm; bed height 10 mm; V_{bed} = 3.14 mL) was packed with pressed nano-$CaCO_3$ and nano-$Mg(OH)_2$ (bed mass 1.6 g; porosity ε = 0.45). The influent contained Cu(II) at 1.0 mg/L. The flow rate was 3.0 mL/min, giving an empty-bed contact time (EBCT) of 1.05 min. Effluent was sampled at intervals and analyzed by ICP-MS. This was operated with a 0.40 mL/min sample uptake; for each sample, the sequence was 30 s uptake, 30 s stabilization, three 30 s acquisitions, and a 45 s rinse with 2% HNO_3, giving 3 min total per sample with 1 mL consumption.

Cycling stability was evaluated by dissolving the spent adsorbent in 0.1 mol/L HCl to recover metals, re-synthesising the adsorbent electrochemically, and re-packing the column; consecutive adsorption–regeneration–reuse cycles were performed under the same flow and influent conditions. Effluent Cu(II) was monitored in each run.

The adsorption capacity of the adsorbent for target metal ions was calculated using Equation (1):

$$q_t = \frac{(C_0 - C_t)V}{W} \tag{1}$$

where q_t (mg/g) denotes the adsorption capacity at time t, C_0 and C_t (mg/L) represent the initial and time-dependent metal ion concentrations, respectively, V (L) is the solution volume, and W (g) is the adsorbent mass [9].

The adsorption equilibrium behavior was analyzed using Langmuir and Freundlich isotherm models. The Langmuir isotherm (Equation (2)) is expressed as:

$$q_e = \frac{q_m K_L C_e}{1 + K_L C_e} \tag{2}$$

The Freundlich isotherm (Equation (3)) is defined as:

$$q_e = K_F {C_e}^{1/n} \tag{3}$$

where q_e (mg/g) is the equilibrium adsorption capacity, q_m (mg/g) is the theoretical maximum capacity, K_L (L/mg) is the Langmuir constant reflecting adsorption affinity, and C_e (mg/L) is the equilibrium metal ion concentration. K_F (mg/g) and n represent adsorption capacity and intensity, respectively [17].

Adsorption kinetics were evaluated using pseudo-first-order (Equation (4)) and pseudo-second-order (Equation (5)) models:

$$\log(q_e - q_t) = \log q_e - \frac{tk_1}{2.303} \quad (4)$$

$$\frac{t}{q_t} = \frac{1}{k_2 q_e^2} + \frac{t}{q_e} \quad (5)$$

where, q_e and q_t (mg/g) are the amounts of heavy metal ions adsorbed at equilibrium and at time t (min), respectively, k_1 (/min) and k_2 (g/mg/min) are the adsorption rate constant of first-order adsorption and the rate constant of second-order adsorption, respectively. The rate constants k_1 and k_2 are determined by plotting log ($q_e - q_t$) versus t and t/q_t versus t, respectively.

2.6. Life Cycle Assessment Method

The life cycle assessment (LCA) of the electrochemical extraction route was conducted by ISO 14040 and 14044 standards (Method S1). The system boundary included the entire process from seawater collection to heavy metal removal application. The functional unit was defined as "production of 1 kg of mixed adsorbent for the treatment of heavy metal-containing wastewater". Data sources included laboratory measurements, literature, and the Ecoinvent database. The environmental impact assessment was based on the ReCiPe 2016 midpoint method. The environmental impacts of the electrochemical route were compared with those of conventional production methods.

3. Results and Discussion

3.1. Structural and Morphological Characterization of Nano-$CaCO_3$ and Nano-$Mg(OH)_2$

Systematic characterization first examined the morphological features of precipitates extracted from seawater using scanning electron microscopy (SEM). As shown in Figures 1b and S7a, the first stage of precipitation exhibited a cubic nanostructure, with crystals neatly arranged and diameters that ranged from 50 to 200 nm. Figures 1c and S7b revealed that the second-stage precipitate displayed typical nano-sheet layered structures, which interwove to form three-dimensional networks, providing abundant surface active sites. These nanoscale morphologies offered large specific surface areas for both materials, which were favorable for enhancing contact and interaction with heavy metal ions.

Fourier transform infrared spectroscopy (FTIR) analysis further confirmed the chemical structures of the precipitates. As illustrated in Figure 1d, the precipitate recovered in the first stage showed distinct absorption peaks at 713/cm and 875/cm, confirming the presence of carbonate structures. The precipitate recovered in the second stage displayed a strong absorption peak near 3699/cm, attributed to the stretching vibration of surface hydroxyl groups, along with additional characteristic peaks at 453/cm (Mg–O stretching vibration) and 1579/cm (H–O–H bending vibration of adsorbed water molecules), which collectively confirm the brucite structure and surface characteristics. These abundant surface functional groups provide multiple binding sites for heavy metal ions, with carbonate groups capable of forming coordination complexes through their electron-rich oxygen atoms, while hydroxy groups can participate in both electrostatic interactions and ligand exchange reactions with metal cations [18].

X-ray photoelectron spectroscopy (XPS) analysis revealed the chemical states of the precipitates (Figures 1e and S8). The survey spectrum of the first-stage precipitate showed distinct signals at binding energies of C 1s, Ca 2p, and O 1s, characteristic of surface-bound carbonate species. The coexistence of C–O and Ca-related peaks suggested the presence of a carbonate structure. For the second-stage precipitate, the XPS spectrum exhibited clear peaks at O 1s and Mg 1s, indicating the existence of hydroxyl and magnesium species. The high intensity of the O 1s peak further supported the abundance of surface hydroxyl groups, pointing to a hydroxide-rich composition. These surface chemical environments create electron-rich regions around oxygen atoms, which serve as strong coordination sites for metal cations through electrostatic attraction and coordination bonding [19]. The high surface density of these reactive species, as evidenced by the intense XPS signals, provides numerous accessible binding sites that facilitate efficient heavy metal ion capture and retention.

Combined with X-ray diffraction (XRD) analysis results (Figure 1f), the first-stage precipitate showed characteristic diffraction peaks at 2θ = 23.1°, 29.5°, 36.0°, 39.5°, 43.2°, and 47.7°, which matched well with the standard calcite phase $CaCO_3$. The second-stage precipitate displayed diffraction peaks at 2θ = 18.5°, 38.0°, 50.8°, and 58.6°, corresponding to the standard brucite phase $Mg(OH)_2$. The sharp and well-defined diffraction patterns indicated high phase purity and excellent crystallinity for both precipitates. The high crystallinity ensures uniform distribution of surface active sites and consistent adsorption behavior, while the excellent phase purity eliminates interference from impurities that could compromise adsorption performance [20,21]. Moreover, the well-ordered crystal structures of calcite and brucite phases provide stable frameworks that maintain structural integrity during

the adsorption process, ensuring reproducible and reliable heavy metal removal efficiency over multiple adsorption-desorption cycles.

Finally, EDS (Figure S9) provided the surface composition (semi-quantitative). On the surface, nano-$CaCO_3$ contained 98.4% Ca, and nano-$Mg(OH)_2$ contained 99.4% Mg (Figure 1g), consistent with the phases identified by XRD/FTIR, both significantly exceeding the 93% required by Chinese industrial standards (HG/T 3249-2001 and HG/T 3607-2007) [22,23]. Subsequently, the structural characteristics of $CaCO_3$ and $Mg(OH)_2$ were tested. These morphological features, combined with nitrogen adsorption-desorption isotherms (Figure 1h), further corroborated their hierarchical porosity. Both precipitates exhibited Type IV isotherms with obvious hysteresis loops at high relative pressures, indicating the presence of mesopores. Notably, $CaCO_3$ and $Mg(OH)_2$ samples possessed a high specific surface area (50.4 m^2/g and 109.8 m^2/g) and pore volume, with dominant pore sizes of 10–50 nm (Figure 1i). Such structural advantages (enhanced surface reactivity, rapid mass transfer kinetics, and abundant accessible active sites) collectively rationalize their exceptional adsorption capacities for heavy metal ions [24], positioning them as high-performance candidates for sustainable water purification.

We further investigated the effects of current density and pH on precipitation at a fixed residence time of 3 min. For $CaCO_3$ (0.1, 0.5, and 1.0 mA/cm^2; Figure S10a–c), a current density of 0.1 mA/cm^2 produced only sparse nanoparticles. At 0.5 mA/cm^2, a more uniform and well-dispersed nano-$CaCO_3$ was obtained. When the current density increased to mA/cm^2, the nano-$CaCO_3$ particles grew rapidly and aggregated, resulting in the loss of their nanostructure. For $Mg(OH)_2$ (10, 15, and 20 mA/cm^2; Figure S10d–f), increasing the current density and pH made the nanosheet network thicker and denser, accompanied by partial stacking and local collapse. The N_2 adsorption–desorption results were consistent with these observations (Figure S11). At lower current densities, both materials exhibited type IV hysteresis with mesoporous structures. $Mg(OH)_2$ showed a higher total adsorption and BET surface area, with pores mainly distributed at 5–20 nm, while $CaCO_3$ exhibited larger and more dispersed pores (20–60 nm). At higher current densities, $Mg(OH)_2$ developed a denser network with slightly shifted mesoporous peaks, whereas $CaCO_3$ showed reduced surface area and pore volume due to agglomeration. Therefore, a current density of 0.5 mA/cm^2 was selected to produce nano-$CaCO_3$, and mA/cm^2 was used to produce nano-$Mg(OH)_2$.

3.2. Adsorption Performance for Heavy Metals

The adsorption performance of the synthesized nano-$CaCO_3$ and nano-$Mg(OH)_2$ for Cu(II), Pb(II), Cd(II), and Cr(III) ions was systematically investigated due to their environmental hazards. Preliminary adsorbent dosage studies demonstrated (Figure S12) an inverse relationship between adsorbent concentration and unit adsorption capacity, with higher capacities achieved at lower dosages due to better site utilization and reduced competition for metal ions. As shown in Figure 2a,b, both materials exhibited adsorption isotherms that were well described by the Langmuir model, with correlation coefficients exceeding 0.99. This result confirmed monolayer adsorption on homogeneously distributed active sites. For Cu(II), $Mg(OH)_2$ demonstrated a superior maximum capacity of 1331.0 mg/g compared to $CaCO_3$ (1113.6 mg/g), attributed to its higher surface area and hydroxyl group abundance, which enhanced coordination with Cu(II). Similar trends were observed for Pb(II), where $Mg(OH)_2$ achieved an exceptional capacity of 3696.8 mg/g (nearly double that of $CaCO_3$ (2180.5 mg/g)), reflecting the strong affinity of Pb(II) for alkaline adsorbents. Cd(II) adsorption capacities followed this pattern, with $Mg(OH)_2$ (1997.4 mg/g) outperforming $CaCO_3$ (1065.3 mg/g), while Cr(III) exhibited lower but still significant uptake ($Mg(OH)_2$: 675.0 mg/g, $CaCO_3$: 637.5 mg/g). The hierarchy of adsorption efficiency (Pb(II) > Cd(II) > Cu(II) > Cr(III)) aligned with ionic properties such as hydration energy and charge density, where the layered nanosheet structure and mesoporosity (10–50 nm pores) of $Mg(OH)_2$ facilitated rapid mass transfer and active site accessibility.

Further investigation across different initial concentrations revealed distinct adsorption mechanisms. As Figure S13 showed, at high concentrations (500 mg/L), nano-$Mg(OH)_2$ achieved remarkable adsorption capacities of 920.34, 925.67, 879.49, and 728.91 mg/g for Pb(II), Cd(II), Cu(II), and Cr(III), respectively, demonstrating chemisorption behavior characterized by strong chemical bonding between metal ions and surface functional groups through coordination complexation and ion exchange mechanisms and particularly favoring Pb(II) due to its larger ionic radius and lower hydration energy. In contrast, at low concentrations (1.0 mg/L), the adsorption capacities decreased significantly to 2.0 mg/g for all metals, indicating a transition to physisorption mechanisms dominated by van der Waals forces, electrostatic interactions, and surface diffusion processes within the mesoporous framework [25]. The dual adsorption mechanism enables effective heavy metal removal across a wide concentration range, making both materials versatile adsorbents for various wastewater treatment applications.

Importantly, the adsorption capacities reported in this study surpass those of existing adsorbents documented in the literature [26–38] (Figure 2c), demonstrating the exceptional heavy metal adsorption performance of nano-$CaCO_3$ and nano-$Mg(OH)_2$ recovered from seawater.

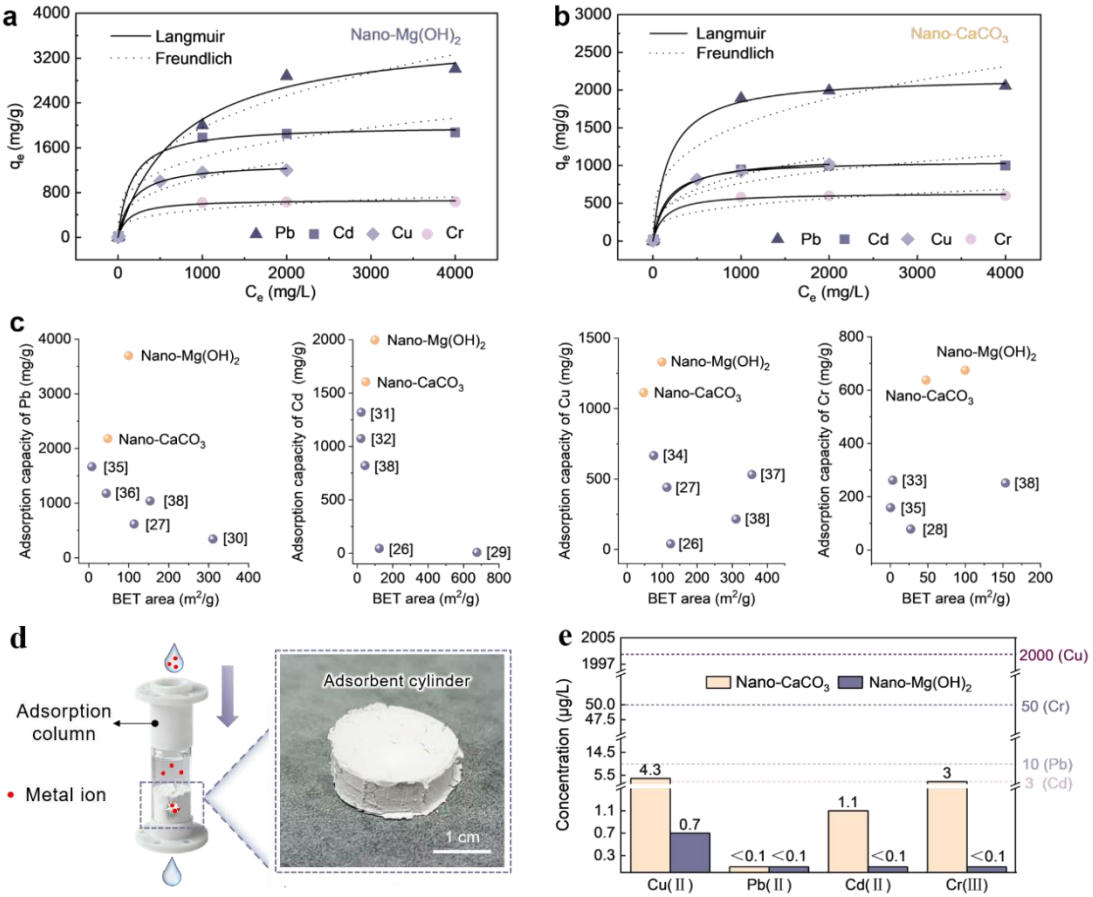

Figure 2. Adsorption isotherms for the sorption of Cu(II), Pb(II), Cd(II), and Cr(III) and fitted models by (**a**) nano-$Mg(OH)_2$ and (**b**) nano-$CaCO_3$; (**c**) Comparison of heavy metal adsorption performance for Pb(II), Cd(II), Cu(II), and Cr(III) ions between the nanomaterials developed in this study and those reported in the literature; (**d**) Photographs of the packed bed setup and adsorbent cylinder; (**e**) The residual metal concentration in effluent after passing through the packed bed. Dashed lines correspond to the upper limits of metal concentration in the drinking water standards of the World Health Organization.

Removing trace metal ions from aqueous solutions remains a significant challenge due to their low concentrations and persistent environmental risks. However, nano-$CaCO_3$ and nano-$Mg(OH)_2$, due to their nanoscale dimensions and abundant porous structures, offer potential solutions to this challenge. To evaluate their performance in trace metal removal, the nanoparticles were compacted into cylindrical packing materials to construct a packed bed (Figure 2d) with enhanced mass transfer capabilities. For the solution with initial Cu(II), Pb(II), Cd(II) and Cr(III) ion concentration of 1000 μg/L, when nano-$CaCO_3$ served as adsorbent cylinder, the effluent concentrations of Cu(II), Pb(II), Cd(II), and Cr(III) dropped to 4.3 μg/L, <0.1 μg/L, 1.1 μg/L, and <0.1 μg/L, respectively. Using nano-$Mg(OH)_2$ as the adsorbent cylinder further improved performance, reducing all four metal ions to ≤0.7 μg/L (Cu(II): 0.7 μg/L; Pb(II), Cd(II), Cr(III): <0.1 μg/L) (Figure 2e). Significantly, these values are well below the World Health Organization's drinking water standards (Pb(II) < 10 μg/L, Cd(II) < 3 μg/L, total Cr(III) < 50 μg/L, and Cu(II) < 2000 μg/L), demonstrating the exceptional capacity of seawater-derived nanoparticles to adsorb trace metals. To verify the long-term stability of the packed bed, we used a $Mg(OH)_2$-based packed bed to adsorb a 1.0 mg/L Cu(II) solution. As shown in Figure S14, the Cu(II) concentration in the effluent remained consistently below 0.7 μg/L for 160 h, demonstrating the packed bed's ability to maintain stable and continuous operation over an extended period.

Under the same batch conditions as the adsorption tests (100 mL; 0.5 g/L), acid dissolution followed by pH-controlled reprecipitation gave mother-liquor residuals of Pb(II) = 0.06 mg/L, Cr(III) = 0.03 mg/L, Cu(II) = 3.04 mg/L, and Cd(II) = 10.11 mg/L (Figure S15). Using the q_{max} values reported in this work, the corresponding metal recoveries were Pb(II) ≥ 99.99%, Cr(III) ≥ 99.97%, Cu(II) = 99.50%, and Cd(II) = 99.0%. It has been proven that our adsorbent not only has excellent adsorption capacity, but also possesses good metal recovery capability.

Under the same packed bed conditions, three independently prepared $CaCO_3$ and three $Mg(OH)_2$ columns all kept the effluent Cu(II) ≤ 0.7 μg/L (Figure S16), with $Mg(OH)_2$ generally giving lower values than $CaCO_3$. This demonstrates good batch-to-batch reproducibility in material preparation and packing.

After acid dissolution (0.1 mol/L HCl), electrochemical re-synthesis and re-packing, three consecutive adsorption–regeneration–reuse cycles still met ≤ 0.7 μg/L in the effluent (Figure S17). No noticeable increase in pressure drop or signs of channeling were observed.

3.3. Adsorption Mechanisms

To comprehensively understand the adsorption mechanisms of nano-$CaCO_3$ and nano-$Mg(OH)_2$ for Cu(II), Pb(II), Cd(II), and Cr(III), the adsorption process was analyzed in detail using the fitting results of the Langmuir and Freundlich isotherm models, as well as the pseudo-first-order and pseudo-second-order kinetic models [39,40]. Because our equilibrium data fall in a low-concentration, low-coverage region far from saturation, Langmuir and Freundlich behave nearly linearly and therefore yield very similar goodness of fit.

The adsorption of Cu(II) on both nano-$CaCO_3$ and nano-$Mg(OH)_2$ demonstrated strong adsorption capacities. The isotherm fitting results indicate that the adsorption of Cu(II) follows the Langmuir model (Table 1), suggesting monolayer adsorption on homogeneous adsorption sites. The maximum adsorption capacities for Cu(II) were 1331.0 mg/g for nano-$Mg(OH)_2$ and 1113.6 mg/g for nano-$CaCO_3$, showing that $Mg(OH)_2$ exhibits superior adsorption performance compared to $CaCO_3$. This can be attributed to the greater abundance of hydroxyl groups and the larger specific surface area of $Mg(OH)_2$, which facilitates stronger coordination interactions with Cu(II) ions. At the molecular level, Cu(II) adsorption on $Mg(OH)_2$ involves inner-sphere complexation, where Cu(II) directly coordinates with surface hydroxyl groups, forming stable Cu-O bonds. The electron configuration of Cu(II) ($3d^9$) enables the formation of coordination complexes with electron-rich hydroxyl groups [41]. For $CaCO_3$, the adsorption likely occurs through both complexation with carbonate groups and potential surface precipitation of copper species at the solid-liquid interface.

Table 1. Isotherm parameters of the Langmuir and the Freundlich models for Cu(II), Pb(II), Cd(II), and Cr(III) of nano-$CaCO_3$ and nano-$Mg(OH)_2$.

Adsorbent Type	Adsorbate	Langmuir Model			Freundlich Mode		
		q_m/(mg/g)	R^2	K_L/(L/mg)	K_F/(mg/g)	R^2	n
Nano-$CaCO_3$	Cu(II)	1113.6	0.996	0.00513	81.5	0.929	2.91
Nano-$CaCO_3$	Pb(II)	2180.5	0.994	0.00543	200.9	0.902	3.40
Nano-$CaCO_3$	Cd(II)	1065.3	0.993	0.00638	107.3	0.894	3.51
Nano-$CaCO_3$	Cr(III)	637.5	0.993	0.00735	68.1	0.892	3.61
Nano-$Mg(OH)_2$	Cu(II)	1331.0	0.993	0.00583	106.4	0.913	3.00
Nano-$Mg(OH)_2$	Pb(II)	3696.8	0.984	0.00132	152.9	0.954	2.71
Nano-$Mg(OH)_2$	Cd(II)	1997.4	0.994	0.00623	189.8	0.889	3.48
Nano-$Mg(OH)_2$	Cr(III)	675.0	0.990	0.00785	68.6	0.887	3.63

Similar to Cu(II), the adsorption of Pb(II), Cd(II), and Cr(III) on nano-$CaCO_3$ and nano-$Mg(OH)_2$ also follows the Langmuir isotherm model, indicating monolayer adsorption. Among these metals, Pb(II) exhibited the strongest adsorption capacity, with maximum adsorption capacities of 3696.8 mg/g for nano-$Mg(OH)_2$ and 2180.5 mg/g for nano-$CaCO_3$ (Table 1). The exceptional affinity for Pb(II) can be explained by Hard-Soft Acid-Base (HSAB) theory and ionic properties. Pb(II), with its $6s^2$ lone pair electrons, behaves as a borderline acid that interacts effectively with both hydroxyl groups in $Mg(OH)_2$ and carbonate groups in $CaCO_3$. Additionally, Pb(II) has a larger ionic radius (119 pm) compared to Cu(II) (73 pm), Cd(II) (95 pm), and Cr(III) (62 pm), resulting in lower hydration energy and facilitating easier dehydration during adsorption, which contributes to its higher adsorption capacity [42].

The observed adsorption hierarchy (Pb(II) > Cd(II) > Cu(II) > Cr(III)) correlates well with the interplay between hydration energies and electronegativity values. The hydration strength decreases in the order: Cr(III) (−4563 kJ/mol) > Cu(II) (−2121 kJ/mol) > Cd(II) (−1828 kJ/mol) > Pb(II) (−1502 kJ/mol). while electronegativity values are: Pb(II) (2.33) > Cu(II) (1.90) > Cd(II) (1.69) > Cr(III) (1.66) [39,43,44]. Pb(II) benefits from both the lowest hydration energy and highest electronegativity, facilitating easy dehydration and strong surface coordination. The dominant factor appears to be the balance between these properties, where dehydration barriers often outweigh pure electrostatic effects [45].

In contrast, the adsorption capacity for Cr(III) was lower, with 675.0 mg/g for $Mg(OH)_2$ and 637.5 mg/g for $CaCO_3$. The lower adsorption capacity for Cr(III) can be attributed to its smaller ionic radius, higher charge density, and stronger hydration shell, which creates an energy barrier for effective surface interactions. Cr(III) typically

forms stable octahedral complexes $[Cr(H_2O)_6]^{3+}$ in solution that must be partially disrupted for adsorption to occur [46,47].

Further kinetic analysis shows that the adsorption of Cu(II), Pb(II), Cd(II), and Cr(III) for nano-$CaCO_3$ and nano-$Mg(OH)_2$ all follow the pseudo-second-order kinetic model (Figure 3a and Table 2). This suggests that the adsorption of metal ions is influenced not only by concentration but also by surface site exchange and ion diffusion. And chemisorption is the rate-limiting step in the adsorption process, involving valence forces through sharing or exchange of electrons between metal ions and adsorbent surface groups.

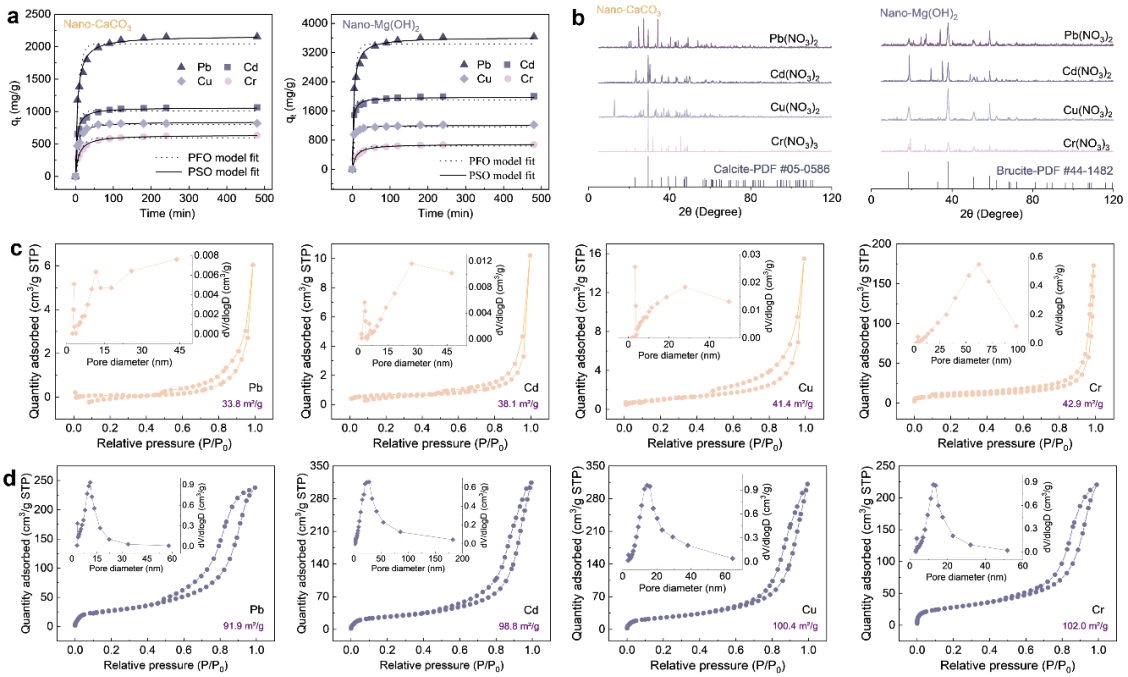

Figure 3. (**a**) Adsorption kinetics for the sorption of Pb(II), Cd(II), Cu(II), and Cr(III) and fitted models by nano-$CaCO_3$ and nano-$Mg(OH)_2$; (**b**) XRD patterns of nano-$CaCO_3$ and nano-$Mg(OH)_2$ after heavy metal adsorption; N_2 adsorption-desorption isotherm and pore size distribution of (**c**) nano-$CaCO_3$ and (**d**) nano-$Mg(OH)_2$ after adsorption of Pb(II), Cd(II), Cu(II), and Cr(III).

Table 2. Kinetic parameters of the pseudo-first-order and pseudo-second-order models for Cu(II), Pb(II), Cd(II), and Cr(III) of nano-$CaCO_3$ and nano-$Mg(OH)_2$.

Adsorbent Type	Adsorbate	Pseudo-First-Order Model			Pseudo-Second-Order Model		
		q_e(mg/g)	K_1(/min)	R^2	q_e (mg/g)	K_2(g/mg/min)	R^2
Nano-$CaCO_3$	Cu(II)	798.3	0.12416	0.965	838.2	2.5287×10^{-4}	0.991
Nano-$CaCO_3$	Pb(II)	2043.7	0.11805	0.946	2165.5	8.7888×10^{-5}	0.991
Nano-$CaCO_3$	Cd(II)	1008.6	0.15427	0.952	1061.5	2.4339×10^{-4}	0.993
Nano-$CaCO_3$	Cr(III)	595.2	0.07463	0.958	639.5	1.7625×10^{-4}	0.994
Nano-$Mg(OH)_2$	Cu(II)	1167.7	0.29881	0.976	1203.9	5.3399×10^{-4}	0.996
Nano-$Mg(OH)_2$	Pb(II)	3434.2	0.15519	0.961	3617.4	7.1137×10^{-5}	0.993
Nano-$Mg(OH)_2$	Cd(II)	1908.1	0.26249	0.971	1976.3	2.6396×10^{-4}	0.995
Nano-$Mg(OH)_2$	Cr(III)	639.1	0.06961	0.957	688.8	1.5167×10^{-4}	0.993

Based on the above analysis, the adsorption processes of Cu(II), Pb(II), Cd(II), and Cr(III) by nano-$CaCO_3$ and nano-$Mg(OH)_2$ are primarily influenced by the coordination interactions of surface hydroxyl and carbonate groups. The good fits to the Langmuir and pseudo-second-order kinetic models indicate that the adsorption process is monolayer adsorption with a fast rate, mainly controlled by ion exchange and complexation at surface active sites. For $CaCO_3$, adsorption occurs through carbonate group coordination, where oxygen atoms in CO_3^{2-} groups serve as coordination sites for metal cations, alongside ion exchange of Ca^{2+} ions with heavy metals at surface sites [48,49]. The relatively small capacity difference (16%) between $Mg(OH)_2$ and $CaCO_3$ suggests that surface area-dependent mechanisms such as electrostatic interactions, complexation, and ion exchange contribute significantly to adsorption in both systems, with the surface complexation capacity of carbonate groups approaching that of hydroxyl groups for certain metal ions [50]. Additionally, nano-$Mg(OH)_2$ showed higher

adsorption capacities for metal ions, which may be attributed to its higher number of active sites and larger specific surface area.

Post-adsorption characterization provides further mechanistic insights into metal ion incorporation. XRD analysis (Figure 3b) confirms structural integrity preservation, with $Mg(OH)_2$ maintaining its brucite phase peaks (2θ = 18.5°, 38.0°, 50.8°, 58.6°) and $CaCO_3$ preserving calcite characteristics (2θ = 23.1°, 29.5°, 36.0°, 39.5°, 43.2°, 47.7°) after metal loading. The absence of metal hydroxide or carbonate precipitate phases confirms surface adsorption mechanisms rather than bulk precipitation [51]. XPS analysis (Figures S18–S20) reveals successful metal incorporation with characteristic binding energy shifts: Pb $4f_{7/2}$ (138.7 eV), Cd $3d_{5/2}$ (405.8 eV), Cu $2p_{3/2}$ (933.9 eV), and Cr $2p_{3/2}$ (576.4 eV), showing 0.5–1.2 eV increases compared to free metal ions. These shifts confirm coordination bonding with surface functional groups through inner-sphere complexation, supporting the proposed adsorption mechanisms while maintaining adsorbent structural stability.

Complementary FTIR spectra (Figure S21) show diagnostic, metal-induced changes in surface functional groups. For nano-$Mg(OH)_2$, the sharp ν–OH band at ~3695/cm attenuates and slightly broadens after loading, consistent with inner-sphere binding at surface –OH sites. For nano-$CaCO_3$, the carbonate bands (ν_3 ~1425/cm; ν_2 ~873/cm) exhibit intensity/position changes indicative of coordination at carbonate oxygens. These spectral features corroborate chemical immobilization rather than purely physical adsorption. Together with the XPS spectra (Figures S9–S11), which show the appearance/shift of M–O/M–OH and CO_3^{2-} components after loading, the FTIR changes in Figure S21 point to inner-sphere complexation at surface –OH/CO_3^{2-} sites. Consistently, the XRD patterns (Figure 3b) display no new reflections at the examined loadings; any interfacial precipitates are too sparse and poorly crystalline to produce long-range order, so the data support surface complexation as the dominant pathway with only limited interfacial precipitation.

To verify the changes in the specific surface area and pore structure of nano-$CaCO_3$ and nano-$Mg(OH)_2$ after metal adsorption, N_2 adsorption-desorption isotherms and pore-size distribution analyses were conducted (Figure 3c,d). The results showed that both adsorbents exhibited a marked decrease in adsorption uptake after metal loading, accompanied by partial pore blocking in the mesoporous range (10–50 nm). Specifically, after nano-$Mg(OH)_2$ adsorbed heavy metals, its surface area values decreased by 17.9 (Pb(II)), 11.0 (Cd(II)), 9.4 (Cu(II)), and 7.8 (Cr(III)) m^2/g, while that of nano-$CaCO_3$ decreased by 16.6 (Pb(II)), 12.3 (Cd(II)), 9.0 (Cu(II)), and 7.5 (Cr(III)) m^2/g, both following the order Pb(II) > Cd (II)> Cu(II) > Cr(III). This trend was attributed to the different degrees of occupation of surface and pore sites by the metal ions, indicating that during adsorption, the metals progressively filled the mesoporous surfaces and pore entrances, which hindered N_2 diffusion and led to the observed reductions in surface area and pore volume [52]. Together with the XRD/XPS results, these data support a mechanism of inner-sphere surface complexation with limited interfacial precipitation, while preserving the host crystal frameworks.

3.4. Life Cycle Assessment of Electrochemical System

This study employed a standardized life cycle assessment (LCA) method, based on the ISO 14040/14044 framework, to systematically evaluate the comprehensive environmental benefits of the electrochemical technology for softening and recovering nano-$CaCO_3$ and nano-$Mg(OH)_2$ from seawater. The analysis adopted a cradle-to-gate boundary, with the functional unit defined as the treatment of 1000 kg of seawater (Figure 4a). A complete inventory of resource and energy flows, as well as environmental burdens, was constructed to compare the full life cycle environmental performance of the conventional process and the new electrochemical process.

Based on the carbon emission factor of the Chinese power grid (0.811 kg CO_2eq/kWh), the results (Figure 4b,c) showed that the electrochemical method produced a carbon footprint of 0.074 kg CO_2eq per kilogram of nano-$CaCO_3$ and 1.286 kg CO_2eq per kilogram of nano-$Mg(OH)_2$ under a mixed electric structure. Compared with the conventional chemical precipitation process (0.36 kg CO_2 eq/kg) [53], the carbon emissions for nano-$CaCO_3$ were reduced by approximately 80%. Similarly, when compared with the brine extraction and Magnifin process (1.6–5.2 kg CO_2 eq/kg) [54], the carbon emissions for nano-$Mg(OH)_2$ were reduced by 50–75%. This significant reduction in emissions was mainly attributed to the stoichiometric advantages of the electrochemical process and its "zero chemical reagent" input, which avoided the indirect carbon emissions associated with the production and transport of chemicals in traditional processes.

Energy analysis of the power structure (Figure 4d,e) indicated that the regional energy mix had a decisive influence on the process carbon footprint. When a low-carbon power structure was employed (for example, with 78% nuclear energy in France or 71% renewable energy in Sweden), the carbon footprint of the electrochemical process was further reduced, with the carbon emissions for producing both nano-$CaCO_3$ and nano-$Mg(OH)_2$ decreasing by more than 99%. This finding highlighted the dual environmental benefits of the electrochemical

technology when combined with renewable energy, and provided clear guidance for process optimization: priority should be given to regions with abundant clean energy to achieve near-zero carbon material production.

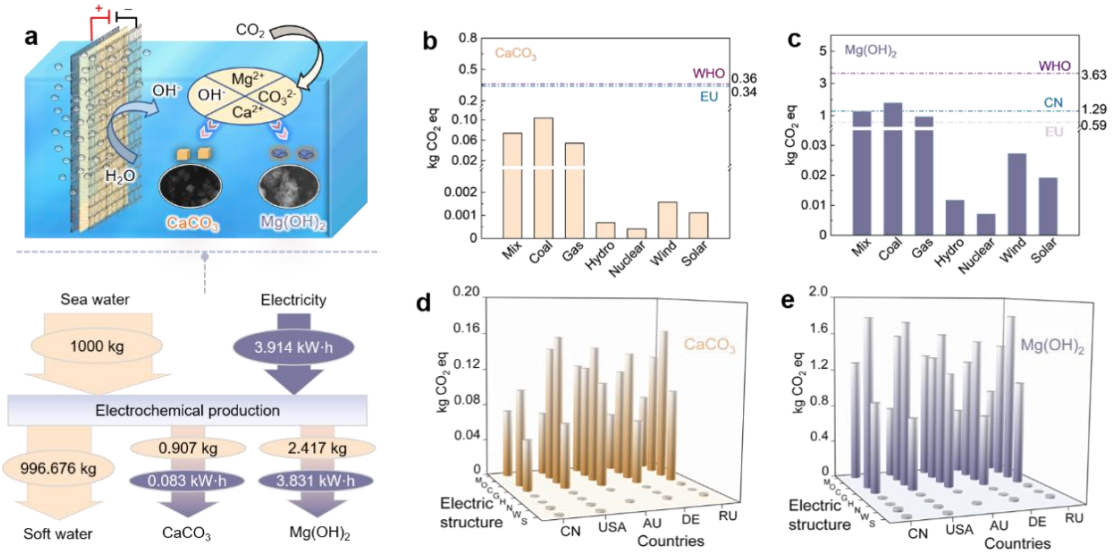

Figure 4. Environmental analysis of nanomaterial production: (**a**) Schematic of the electrochemical production process using seawater to generate $CaCO_3$ and $Mg(OH)_2$; (**b**) Comparative CO_2 emissions for precipitated versus ground calcium carbonate production using different energy sources; (**c**) Comparative CO_2 emissions comparison for magnesium hydroxide versus aluminum hydroxide production across energy sources (the dashed line was the average carbon emissions); Global carbon emissions for (**d**) $CaCO_3$ and (**e**) $Mg(OH)_2$ extraction by electrochemical technology under various electric structures in many countries (M-mix, O-heavy oil, C-coal, G-gas, H-hydro, N-nuclear, W-wind, S-solar).

The multi-dimensional environmental impact assessment employed the ReCiPe 2016 midpoint indicator method. The results showed that the electrochemical process performed superiorly compared with the conventional route in several environmental categories: particulate matter ($PM_{2.5}$) emissions decreased by 55%, fossil resource consumption was reduced by 85%, global warming decreased by 64%, and human health risk was reduced by 70% (Figure 5a). This comprehensive environmental friendliness was attributed to the closed-loop resource feature of the electrochemical process, which converted Ca^{2+} and Mg^{2+} ions from high-salinity wastewater into high-value products while avoiding the environmental burdens associated with the production, transport, and disposal of chemical precipitants in traditional processes.

A comparative analysis for the seawater softening pretreatment scenario (Figures 5b and S22) further revealed differences between the processes. The conventional softening process relied on chemical reagents such as sodium carbonate and sodium hydroxide. For each ton of seawater treated, approximately 0.3–0.5 kg of mixed salt precipitate was produced, which required additional disposal. In contrast, the electrochemical process achieved selective migration and directional crystallization of Ca^{2+} and Mg^{2+} through precise potential control, thereby simultaneously softening the water and recovering $CaCO_3$ and $Mg(OH)_2$. When the substitution benefits of material recovery were taken into account, the net carbon footprint of the electrochemical pretreatment process was −10.428 kg CO_2eq per ton of water. This negative carbon emission, or "carbon sink" effect, aligned closely with national carbon neutrality strategies.

A systematic sensitivity analysis was conducted to evaluate the importance of various factors on environmental impacts. As shown in Figures 5c and S23, in the conventional process, the dosing of chemical reagents and the regional electricity mix were the dominant factors affecting the carbon footprint, with a ±20% variation in these parameters leading to an overall carbon emission change of ±15%. In the electrochemical process, the carbon intensity of electricity was identified as the primary sensitive factor, contributing 76.3% of the overall impact; a ±20% fluctuation in this parameter resulted in a carbon emission change of ±18%, while factors such as electrode efficiency and membrane performance had relatively minor effects. This quantitative assessment provided clear guidance for process optimization: priority should be given to improving energy efficiency and increasing the use of renewable energy to maximize environmental benefits.

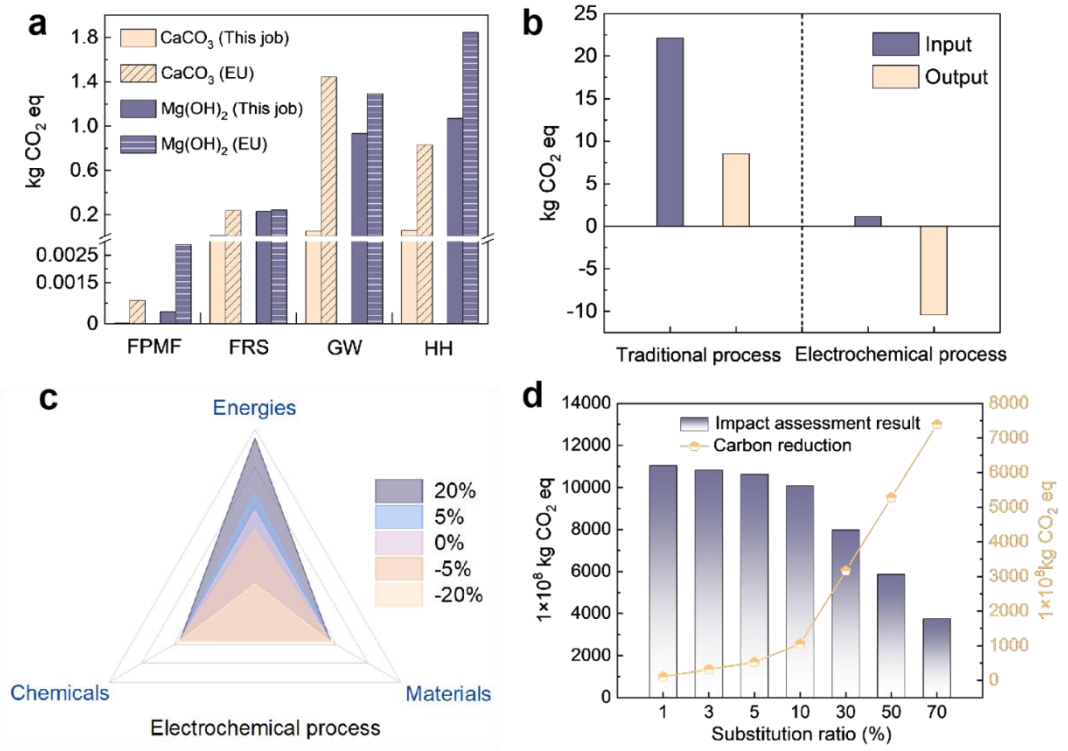

Figure 5. (**a**) Environmental impact comparison between electrochemical and conventional EU processes for $CaCO_3$ and $Mg(OH)_2$ production across impact categories (FPMF-Fine particulate matter formation, FRS-Fossil resource scarcity, GW-Global warming, HH-Human health); (**b**) CO_2 emissions breakdown for traditional and electrochemical processes, showing inputs and outputs for both methods; (**c**) Sensitivity analysis triangles showing the effects of energies, chemicals, and materials input variations on environmental performance of electrochemical processes; (**d**) Carbon emissions and reduction potential when electrochemical process replace traditional process at various substitution ratios.

Based on a scenario simulation using China's annual high-salinity water treatment volume (approximately 50 billion m^3) (Figure 5d), the large-scale application potential was predicted. If the electrochemical process replaced 10% of conventional pretreatment technology, the annual carbon reduction could reach 105.83 billion kg CO_2eq. When the replacement ratio increased to 50%, the annual carbon reduction would rise to 527.91 billion kg CO_2eq, equivalent to the annual carbon sequestration of about 2.4 billion mature trees (each tree sequestering an average of 21.8 kg CO_2 per year). A global analysis of application potential (Figure S24) further demonstrated that the carbon reduction benefits of this technology were positively correlated with local electricity structures. In France and other Nordic countries, greater environmental benefits could be achieved, while in developing regions dominated by coal-fired power, the carbon reduction advantage would gradually emerge as the energy transition progresses, indicating broad prospects for technology adoption.

Comprehensive LCA analysis results indicated that the electrochemical technology for recovering nano-$CaCO_3$ and nano-$Mg(OH)_2$ from seawater possessed significant environmental and economic advantages. Compared with conventional processes, this technology achieved the objectives of "zero chemical reagent input" and "low energy consumption" while converting waste into high-value-added products. Against the backdrop of global decarbonization and a circular economy, this resource recovery technology based on electrochemical principles demonstrated broad application prospects, particularly in coastal regions and high-salinity wastewater treatment, and provided a more environmentally friendly and economical solution.

4. Conclusions

The conventional paradigm for Ca^{2+} and Mg^{2+} recovery from seawater relies on chemical precipitation methods requiring substantial reagents, high-temperature calcination, and complex post-processing. Our research challenges this paradigm by demonstrating that electrochemical homogeneous nucleation can selectively recover valuable minerals under mild conditions without chemical additives, while producing nanomaterials with excellent environmental functionality. Our life cycle assessment approach provides a comprehensive evaluation framework that considers both direct production processes and the synergistic effects of resource recovery and pollution

control. This assessment quantitatively confirms the electrochemical method's significant environmental advantages over traditional processes, particularly in regions with high renewable energy availability.

The nano-scale $CaCO_3$ and nano-scale $Mg(OH)_2$ synthesized through our approach exhibit exceptional adsorption capacities for heavy metals, reducing pollutant concentrations below drinking water standards. This in-situ synthesis strategy under mild conditions significantly reduces treatment costs compared to traditional adsorbent preparation, offering advantages for decentralized water treatment systems and resource-constrained regions. This technology's application extends beyond seawater treatment to high-salinity industrial wastewater and desalination concentrates by adjusting electrochemical parameters, creating a versatile platform for "waste-to-resource" conversion.

Supplementary Materials

The additional data and information can be downloaded at: https://media.sciltp.com/articles/others/25112109 18136279/eChem-25100084-SupplementaryMaterials.pdf. Figure S1: Adsorption kinetics curves of three copper salts using (**a**) nano-$CaCO_3$ and (**b**) nano-$Mg(OH)_2$. Figure S2: Schematic illustration of the mesh electrode module. 1: ruthenium-iridium-titanium anode, 2: nylon net separator, 3: stainless steel mesh cathode, 4: magnetic stirrer. Figure S3: SEM images of $CaCO_3$ collected at (**a**) 1; (**b**) 3; (**c**) 5; (**d**) 10; (**e**) 15; and (**f**) 30 min of electrochemical reaction. Figure S4: The particle size distribution diagrams of $CaCO_3$ particles collected at (**a**) 1; (**b**) 3; (**c**) 5; (**d**) 10; (**e**) 15; and (**f**) 30 min. Figure S5: Thymolphthalein traced bulk dispersion of OH^-, time-lapse images at 70 s, 210 s, and 15 min (total volume 27 L). Figure S6: The pH value of the solution after reaction for 3 min under different current densities. Figure S7: SEM images of (**a**) nano $CaCO_3$ and (**b**) nano $Mg(OH)_2$ at low magnification. Figure S8: XPS spectra of (**a**) Mg 1s and (**b**) Ca 2p of the recycled products. Figure S9: EDS spectra and elemental composition of (**a**) nano-$CaCO_3$ and (**b**) nano-$Mg(OH)_2$. Figure S10: SEM images of (**a–c**) $CaCO_3$ and (**d–f**) $Mg(OH)_2$ collected after 3 min of reaction at different current densities. Figure S11: The N_2 adsorption–desorption curves and pore-size distribution profiles of $CaCO_3$ and $Mg(OH)_2$ precipitates collected after reacting for 3 min under different current densities: (**a**) N_2 adsorption–desorption isotherms at low current densities ($CaCO_3$, 0.1 mA cm^{-2}; $Mg(OH)_2$, 10 mA cm^{-2}); (**b**) corresponding pore-size distributions at low current densities; (**c**) N_2 adsorption–desorption isotherms at high current densities ($CaCO_3$, 1 mA cm^{-2}; $Mg(OH)_2$, 20 mA cm^{-2}); and (**d**) corresponding pore-size distributions at high current densities. Figure S12: Adsorption capacity of (**a**) nano-$CaCO_3$ and (**b**) nano-$Mg(OH)_2$ over time at different initial concentrations. Figure S13: The adsorption effect of nano-magnesium hydroxide on (**a**) Pb(II); (**b**) Cd(II); (**c**) Cu(II); and (**d**) Cr(III) of different concentrations. Figure S14: Breakthrough behavior of Cu^{2+} in a nano-$Mg(OH)_2$ packed bed. Figure S15: The concentration of metals in the solution after acidifying and adjusting the pH with nano-$Mg(OH)_2$. Figure S16: Evaluation of the repeatability of the packed bed. Figure S17: Evaluation of the cycling stability of the packed bed. Figure S18: XPS patterns of (**a**) nano-$CaCO_3$ and (**b**) nano-$Mg(OH)_2$ after heavy metal adsorption. Figure S19: XPS convolution fitting spectra of nano-$Mg(OH)_2$ after adsorption of four heavy metal ions. (**a**) Pb 4f orbital; (**b**) Cd 3d orbital; (**c**) Cr 2p orbital; (**d**) Cu 2p orbital. Figure S20: XPS convolution fitting spectra of nano-$CaCO_3$ after adsorption of four heavy metal ions. (**a**) Pb 4f orbital; (**b**) Cd 3d orbital; (**c**) Cr 2p orbital; (**d**) Cu 2p orbital. Figure S21: Comparison of FTIR patterns of (**a**) nano-$Mg(OH)_2$ and (**b**) nano-$CaCO_3$ after the adsorption of four heavy metal ions. Figure S22: (**a**) Traditional mining processes of $CaCO_3$; (**b**) Flow chart of electrochemical technology as a new technology to replace the pretreatment stage in the saline wastewater treatment process. Figure S23: Sensitivity analysis triangles showing the effects of energies, chemicals, and materials input variations on the environmental performance of the traditional process. Figure S24: Global prediction of carbon emissions for electrochemical preparation of $CaCO_3$ under various power systems in the world. Table S1: Water quality parameters of the East China Sea. Table S2: Detailed information about the ICP-MS instrument. References [55–58] are cited in the supplementary materials.

Author Contributions

Y.Z. (Yuchen Zhao): writing—original draft, visualization, methodology, investigation, formal analysis, data curation, conceptualization; W.K.: conceptualization, writing—review & editing, supervision, project administration, funding acquisition; S.X.: investigation, methodology, data curation; Y.R.: writing—review & editing, methodology, investigation, data curation; X.Z.: methodology, investigation, data curation; W.W.: investigation, methodology, validation; Y.Z. (Yongqian Zhang): methodology, validation; H.Y.: conceptualization, resources, supervision, project administration, funding acquisition, writing—review & editing; G.Z.: writing—review & editing, supervision, validation, formal analysis. All authors have read and agreed to the published version of the manuscript.

Funding

This research was funded by the National Natural Science Foundation of China under Grant Number U22A20241, the Sinopec project under Grant Number 323007, the National Natural Science Foundation of China under Grant Number 52500080, the Postdoctoral Fellowship Program of CPSF under Grant Number GZB20250313, and the China Postdoctoral Science Foundation under Grant Number 2025M771231.

Data Availability Statement

Data will be made available on request.

Conflicts of Interest

The authors declare no conflict of interest.

Use of AI and AI-Assisted Technologies

No AI tools were utilized for this paper.

References

1. Liu, S.; Sun, Q.; Xu, N.; et al. Recent advances in the treatment of heavy/precious metal pollution, resource recovery and reutilization: Progress and perspective. *Coord. Chem. Rev.* **2025**, *523*, 216268.
2. Maierdan, Y.; Gu, K.; Chen, B.; et al. Recycling of heavy-metal-contaminated river sludge into unfired green bricks: Strength, water resistance, and heavy-metals leaching behavior-A laboratory simulation study. *J. Clean. Prod.* **2022**, *342*, 130882.
3. Bielski, A.; Zielina, M.; Młyńska, A. Analysis of heavy metals leaching from internal pipe cement coating into potable water. *J. Clean. Prod.* **2020**, *265*, 121425.
4. Shrestha, R.; Ban, S.; Devkota, S.; et al. Technological trends in heavy metals removal from industrial wastewater: A review. *J. Environ. Chem. Eng.* **2021**, *9*, 105688.
5. Yang, L.; Hu, W.; Chang, Z.; et al. Electrochemical recovery and high value-added reutilization of heavy metal ions from wastewater: Recent advances and future trends. *Environ. Int.* **2021**, *152*, 106512.
6. Zhao, X.; Dong, S.; Wang, H.; et al. Preparation of porous calcium carbonate biochar and its beryllium adsorption performance. *J. Environ. Chem. Eng.* **2023**, *11*, 110102.
7. Jiang, D.; Yang, Y.; Huang, C.; et al. Removal of the heavy metal ion nickel(II) via an adsorption method using flower globular magnesium hydroxide. *J. Hazard. Mater.* **2019**, *373*, 131–140.
8. Falyouna, O.; Bensaida, K.; Maamoun, I.; et al. Synthesis of hybrid magnesium hydroxide/magnesium oxide nanorods [$Mg(OH)_2$/MgO] for prompt and efficient adsorption of ciprofloxacin from aqueous solutions. *J. Clean. Prod.* **2022**, *342*, 130949.
9. Feng, Y.; Liu, W.; Mu, C.; et al. Highly effective Pb(II) adsorption using physical-chemical double crosslinked polyvinyl alcohol-coated nano-calcium carbonate aerogel beads. *Chem. Phys. Lett.* **2025**, *861*, 141832.
10. Zhu, H.; Li, L.; Chen, W.; et al. Controllable synthesis of coral-like hierarchical porous magnesium hydroxide with various surface area and pore volume for lead and cadmium ion adsorption. *J. Hazard. Mater.* **2021**, *416*, 125922.
11. Rolfe, A.; Huang, Y.; Haaf, M.; et al. Technical and environmental study of calcium carbonate looping versus oxy-fuel options for low CO_2 emission cement plants. *Int. J. Greenh. Gas Control.* **2018**, *75*, 85–97.
12. Yam, B.J.Y.; Le, D.K.; Do, N.H.; et al. Recycling of magnesium waste into magnesium hydroxide aerogels. *J. Environ. Chem. Eng.* **2020**, *8*, 104101.
13. Gude, V.G. Geothermal source potential for water desalination-Current status and future perspective. *Renew. Sustain. Energy Rev.* **2016**, *57*, 1038–1065.
14. Khodadousti, S.; Kolliopoulos, G. Batteries in desalination: A review of emerging electrochemical desalination technologies. *Desalination* **2024**, *573*, 117202.
15. Meng, G.; Xu, J.; Cheng, R.; et al. Controllable synthesis and characterization of high-purity calcium carbonate whisker-like fibers by electrochemical cathodic reduction method. *J. Clean. Prod.* **2022**, *342*, 130923.
16. Lei, Y.; Hidayat, I.; Saakes, M.; et al. Fate of calcium, magnesium and inorganic carbon in electrochemical phosphorus recovery from domestic wastewater. *Chem. Eng. J.* **2019**, *362*, 453–459.
17. Liao, Z.; Wu, S.; Zhang, H.; et al. Removal of aqueous Cu^{2+} by amorphous calcium carbonate: Efficiency and mechanism. *Minerals* **2022**, *12*, 362.
18. Rouff, A.A.; Elzinga, E.J.; Reeder, R.J.; et al. X-ray absorption spectroscopic evidence for the formation of Pb(II) inner-sphere adsorption complexes and precipitates at the calcite-water interface. *Environ. Sci. Technol.* **2004**, *38*, 1700–1707.

19. Brown, G.E., Jr.; Foster, A.L.; Ostergren, J.D. Mineral surfaces and bioavailability of heavy metals: A molecular-scale perspective. *Proc. Natl. Acad. Sci. USA* **1999**, *96*, 3388–3395.
20. Henrist, C.; Mathieu, J.P.; Vogels, C.; et al. Morphological study of magnesium hydroxide nanoparticles precipitated in dilute aqueous solution. *J. Cryst. Growth* **2003**, *252*, 176–187.
21. Yan, H.; Zhang, X.H.; Wu, J.M.; et al. The use of CTAB to improve the crystallinity and dispersibility of ultrafine magnesium hydroxide by hydrothermal route. *Mater. Lett.* **2008**, *62*, 2483–2486.
22. *HG/T 3249-2001*; Industrial Heavy Calcium Carbonate (in Chinese). Chemical Industry Standard of PRC: Beijing, China, 2001.
23. *HG/T 3607-2007*; Magnesium Hydroxide for Industrial Use (in Chinese). Chemical Industry Standard of PRC: Beijing, China, 2007.
24. Tang, X.-J.; Du, Z.-Y.; Zhu, Y.-M.; et al. Correlation between microstructure and dissolution property of magnesium hydroxide synthesized via magnesia hydroxylation: Effect of hydration agents. *J. Clean. Prod.* **2020**, *249*, 119371.
25. Murphy, O.P.; Vashishtha, M.; Palanisamy, P.; et al. A review on the adsorption isotherms and design calculations for the optimization of adsorbent mass and contact time. *ACS Omega* **2023**, *8*, 17407–17430.
26. Zhang, M.; Song, W.; Chen, Q.; et al. One-pot synthesis of magnetic Ni@$Mg(OH)_2$ core-shell nanocomposites as a recyclable removal agent for heavy metals. *ACS Appl. Mater. Interfaces* **2015**, *7*, 1533–1540.
27. Huang, D.; Li, B.; Wu, M.; et al. Graphene oxide-based Fe-Mg(hydr)oxide nanocomposite as heavy-metals adsorbent. *J. Chem. Eng.* **2018**, *63*, 2097–2105.
28. Liu, M.; Wang, Y.; Chen, L.; et al. $Mg(OH)_2$-supported nanoscale zero-valent iron enhancing the removal of Pb(II) from aqueous solution. *ACS Appl. Mater. Interfaces* **2015**, *7*, 7961–7969.
29. Wang, K.; Zhao, J.; Li, H.; et al. Removal of cadmium(II) from aqueous solution by granular activated carbon supported magnesium hydroxide. *J. Taiwan Inst. Chem. Eng.* **2016**, *61*, 287–291.
30. Wang, P.; Ye, Y.; Liang, D.; et al. Layered mesoporous $Mg(OH)_2$/GO nanosheet composite for efficient removal of water contaminants. *RSC Adv.* **2016**, *6*, 26977–26983.
31. Zhang, R.; Richardson, J.J.; Masters, A.F.; et al. Effective removal of toxic heavy metal ions from aqueous solution by $CaCO_3$ microparticles. *Water Air Soil Pollut.* **2018**, *229*, 136.
32. Zhou, X.; Liu, W.; Zhang, J.; et al. Biogenic calcium carbonate with hierarchical organic–inorganic composite structure enhancing the removal of Pb(II) from wastewater. *ACS Appl. Mater. Interfaces* **2017**, *9*, 35785–35793.
33. Merrikhpour, H.; Jalali, M. Waste calcite sludge as an adsorbent for the removal of cadmium, copper, lead, and zinc from aqueous solutions. *Clean Technol. Environ. Policy* **2012**, *14*, 845–855.
34. Mohammadifard, H.; Amiri, M.C. Evaluating Cu(II) removal from aqueous solutions with response surface methodology by using novel synthesized $CaCO_3$ nanoparticles prepared in a colloidal gas aphron system. *Chem. Eng. Commun.* **2017**, *204*, 476–484.
35. Lin, P.Y.; Wu, H.M.; Hsieh, S.L.; et al. Preparation of vaterite calcium carbonate granules from discarded oyster shells as an adsorbent for heavy-metal-ions removal. *Chemosphere* **2020**, *254*, 126903.
36. Zhang, M.; Shen, H.; Qian, Z.; et al. Dual-purpose applications of magnetic phase-change microcapsules with crystalline-phase-tunable $CaCO_3$ shell for waste heat recovery and heavy-metal-ion removal. *J. Energy Storage* **2022**, *55*, 105672.
37. Sun, S.; Tang, Y.; Li, J.; et al. Fly-ash-derived calcium silicate hydrate as a highly efficient and fast adsorbent for Cu(II) ions: Role of copolymer functionalization. *RSC Adv.* **2022**, *12*, 22843–22852.
38. Wang, P.; Shen, T.; Li, X.; et al. Magnetic mesoporous calcium carbonate-based nanocomposites for the removal of toxic Pb(II) and Cd(II) ions from water. *ACS Appl. Nano Mater.* **2020**, *3*, 1272–1281.
39. Velarde, L.; Nabavi, M.S.; Escalera, E.; et al. Adsorption of heavy metals on natural zeolites: A review. *Chemosphere* **2023**, *328*, 138508.
40. Zhou, C.; Wang, X.; Wang, Y.; et al. The sorption of single- and multi-heavy metals in aqueous solution using enhanced nano-hydroxyapatite assisted with ultrasonic. *J. Environ. Chem. Eng.* **2021**, *9*, 105240.
41. Zheng, T.; Fan, H.; Zhao, J.; et al. Tuning electron configuration of metal sites for the diesel adsorptive desulfurization over ion-exchanged zeolite Y. *J. Environ. Chem. Eng.* **2024**, *12*, 113751.
42. Zhao, F.; Cai, H.; Song, Z.; et al. Structural confinement for Cr^{3+} activators toward efficient near-infrared phosphors with suppressed concentration quenching. *Chem. Mater.* **2021**, *33*, 3621–3630.
43. Fan, X.; Liu, H.; Anang, E.; et al. Effects of electronegativity and hydration energy on the selective adsorption of heavy metal ions by synthetic NaX zeolite. *Materials* **2021**, *14*, 4066.
44. Strawn, D.G. Sorption mechanisms of chemicals in soils. *Soil Syst.* **2021**, *5*, 13.
45. Moreno-Castilla, C.; Álvarez-Merino, M.A.; Pastrana-Martínez, L.M.; et al. Adsorption mechanisms of metal cations from water on an oxidized carbon surface. *J. Colloid Interface Sci.* **2010**, *345*, 461–466.
46. Majigsuren, E.; Byambasuren, U.; Bat-Amgalan, M.; et al. Adsorption of chromium(III) and chromium(VI) ions from aqueous solution using chitosan-clay composite materials. *Polymers* **2024**, *16*, 1399.

47. Mohan, D.; Pittman, C.U., Jr. Activated carbons and low-cost adsorbents for remediation of tri- and hexavalent chromium from water. *J. Hazard. Mater.* **2006**, *137*, 762–811.
48. Jin, B.; Wang, S.; Lei, Y.; et al. Green and effective remediation of heavy-metals-contaminated water using $CaCO_3$ vaterite synthesized through biomineralization. *J. Environ. Manag.* **2024**, *353*, 120136.
49. Zhang, M.; Liu, G.; Liu, R.; et al. Efficient flocculation of multiple heavy metals by iron-based modified-carbonate biochar: Adsorption mechanism and practical application. *J. Environ. Chem. Eng.* **2025**, *13*, 115120.
50. Zeng, H.; Jin, B.; Xu, S.; et al. Removal of copper, lead and cadmium from water through enzyme-induced carbonate precipitation by soybean urease. *Environ. Res.* **2025**, *277*, 121610.
51. Ashokan, A.; Sampath Kumar, T.S.; Jayaraman, G. Process optimization for the rapid conversion of calcite into hydroxyapatite microspheres for chromatographic applications. *Sci. Rep.* **2022**, *12*, 12164.
52. Hassan, M.; Liu, Y.; Naidu, R.; et al. Mesoporous biopolymer architecture enhanced the adsorption and selectivity of aqueous heavy-metal ions. *ACS Omega* **2021**, *6*, 15316–15331.
53. Sphera Solutions GmbH. *GaBi LCA Databases & Software: Database Documentation and Electricity Grid Mix Datasets*; Sphera Solutions GmbH: Leinfelden-Echterdingen, Germany, 2024.
54. Luong, V.-T.; Amal, R.; Scott, J.A.; et al. A comparison of carbon footprints of magnesium oxide and magnesium hydroxide produced from conventional processes. *J. Clean. Prod.* **2018**, *202*, 1035–1044.
55. Sphera. Life Cycle Assessment (LCA) Database: Updated, Reliable and Consistent Environmental Data. **2022**. Available online: https://sphera.com/life-cycle-assessment-lca-database (accessed on 10 October 2025).
56. Goedkoop, M.; Oele, M.; Leijting, J.; et al. *ReCiPe 2008: A Life Cycle Impact Assessment Method which Comprises Harmonised Category Indicators at the Midpoint and the Endpoint Level. Report I: Characterisation*; Ministry of Housing, Spatial Planning and Environment (VROM): The Hague, Netherlands, 2009.
57. Huijbregts, M. A. J.; Steinmann, Z. J. N.; Elshout, P. M. F.; et al. ReCiPe2016: A harmonised life cycle impact assessment method at midpoint and endpoint level. *Int. J. Life Cycle Assess.* **2017**, 22, 138–147.
58. Wernet, G.; Bauer, C.; Steubing, B.; et al. The ecoinvent database version 3 (part I): Overview and methodology. *Int. J. Life Cycle Assess.* **2016**, 21, 1218–1230.